Ⓔ

Spiral-Arm Seismic Arrays

by B. L. N. Kennett, J. Stipčević,[*] and A. Gorbatov

Abstract   Seismic arrays have many uses for signal enhancement, from surface-wave characterization of the near surface to teleseismic detection in the context of monitoring nuclear tests. Many variants of the geometrical configuration of stations have been used with the objective of maximizing potential resolution of the incoming wavefronts direction of arrival. A versatile class of array configurations, with good resolution properties, can be constructed with multiple spiral arms. The array response is comparable with the same number of full circles, but with far fewer stations and is robust to minor position changes in emplacement. The desirable properties of the spiral-arm arrays are illustrated for a permanent array in the Precambrian Pilbara craton in northwestern Australia and for a temporary array on ancient sediments in southern Queensland, Australia. In each case, the practical array response is very good and matches the theoretical expectations. The spiral-arm configuration allows the deployment of relatively large aperture arrays with a limited number of stations, which is advantageous in a broad range of seismic applications, including near-surface characterization.

Online Material: Figures illustrating the relation between spiral-arm and multiring circular arrays.

Introduction

Seismic arrays have many uses for signal enhancement, from surface-wave characterization of the near surface to teleseismic detection in the context of monitoring nuclear tests. Such arrays are now commonly employed as a means of signal enhancement, both for detection of weak signals and for identifying the local character of the wavefield. Seismic arrays were introduced in the context of teleseismic detection of underground nuclear tests (e.g., Birtill and Whiteway, 1965) but subsequently have found a wide range of uses, as discussed in the review by Rost and Thomas (2002). Many applications depend on extracting the directional characteristics of portions of the wavefield. Array design represents a compromise between maximizing resolution and constraints on the size of the array and the numbers of available seismometers. Seismic arrays have found applications on many scales, from teleseismic to regional and local.

The shortest wavelengths in the seismic wavefield cannot be recovered directly from array processing due to spatial aliasing. The relation between the interstation distance d and the spatial Nyquist frequency suggests that each wavelength used in the study should be sampled in at least two discrete sampling locations so that the minimum interstation distance should be $d_{\min} = \lambda/2$. The resolution of the array is defined by the capability to separate two waves propagating at closely

spaced wavenumbers and is related to the maximum aperture of the array that should be comparable with $\lambda_{\max}$.

When the wavefront across the group of stations can be approximated by a plane wave characterized by horizontal slowness and azimuth, the array output response is given by the 2D spatial Fourier transform of the pattern of stations shifted to be centered at the parameters of the wavefront. The aperture for which this representation is appropriate depends on frequency, but it works well out to 50 km aperture for 1–2 Hz signals.

The linear array sum for an incident plane wave, with appropriate time delays at the N sensors, takes the form

$$U(\mathbf{s}, \omega) = \frac{1}{N} \sum_{j=1}^{N} u(\mathbf{x}_j, \omega) \exp[-i\omega(\mathbf{x}_j \cdot \mathbf{s})], \qquad (1)$$

in terms of the dot product between the vector slowness $\mathbf{s}$ and the sensor coordinates $\mathbf{x}_j$ relative to a reference site at the origin. For a single plane wave traveling with an azimuth ϕ and an inclination to the vertical i, the slowness vector $\mathbf{s} = s(\cos\phi \sin i, \sin\phi \sin i, \cos i)$. Unless the array has unusually high topographic relief, the vertical contribution $x_{j3} \cos i$ to the time delays is not usually significant.

The action of the summation in equation (1) enhances arrivals with slowness close to $\mathbf{s}$, because these will be coherent across the set of traces. If we represent the wavefield u in the frequency–slowness domain, then the array sum can be written as

---

*Also at the Department of Geophysics, Faculty of Science, University of Zagreb, Zagreb, Croatia.
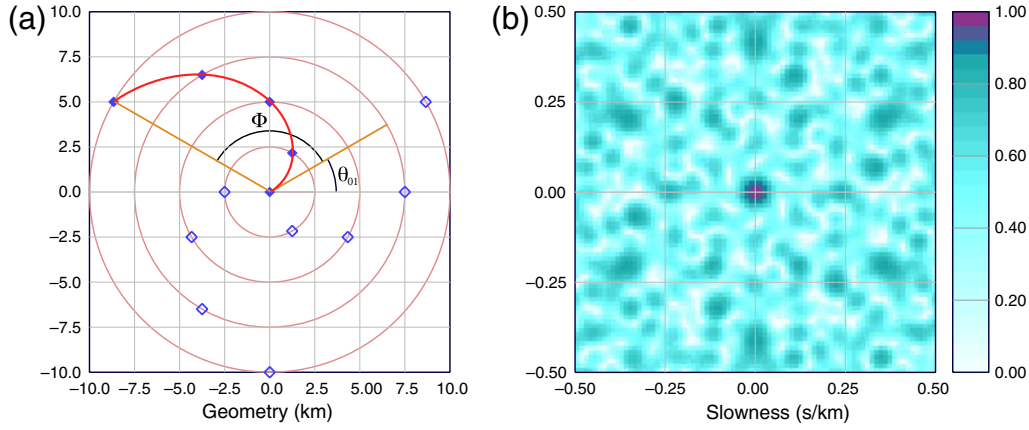
Figure 1. (a) Configuration of a spiral-arm array with a 20 km aperture, three arms, four station rings, and a span Φ of $120°$ for each arm. The rings are indicated, and the spiral configuration underlying one arm is marked with a continuous line. (b) The associated energy response in slowness space for a 1 Hz signal, with a linear scale. The color version of this figure is available only in the electronic edition.

$$U(\mathbf{s}, \omega) = \omega^2 \int_{-\infty}^{\infty} dp_1 \int_{-\infty}^{\infty} dp_2 \, \bar{u}(\mathbf{p}, \omega) \mathcal{S}(\mathbf{p} - \mathbf{s}, \omega). \quad (2)$$

(e.g., Kennett, 2002, chapter 23). The original wavefield is modulated by the array response function $\mathcal{S}(\Delta\mathbf{s}, \omega)$ for the differential slowness $\Delta\mathbf{s} = \mathbf{p} - \mathbf{s}$. The array response function $\mathcal{S}$, sometimes also known as the array transfer function, is given by

$$\mathcal{S}(\Delta\mathbf{s}, \omega) = \frac{1}{N} \sum_{j=1}^{N} \exp\{i\omega[\Delta\mathbf{s} \cdot \mathbf{x}_J]\}. \quad (3)$$

The same functional form is derived irrespective of the slowness $\mathbf{s}$, because the pattern in slowness space is dictated by the geometry of the array. $\mathcal{S}(\Delta\mathbf{s}, \omega)$ is a scaled version of the Fourier transform (with respect to wavenumber) of a set of delta functions placed at the array positions and can be characterized by calculating the array response for a vertically incident wave for which $s_1 = s_2 = 0$.

An alternative representation for the modulus of the array response is given by

$$|\mathcal{S}(\Delta\mathbf{s}, \omega)|^2 = \frac{1}{N^2} \sum_{i=1}^{N} \sum_{j=1}^{N} \exp\{i\omega[\Delta\mathbf{s} \cdot (\mathbf{x}_i - \mathbf{x}_j)]\}, \quad (4)$$

which indicates the important role of the interstation vectors $\mathbf{x}_i - \mathbf{x}_j$.

The array response $|S|$ peaks at zero slowness, and the rate of drop off increases with aperture. Thus, in principle, larger aperture arrays have better slowness resolution provided the signal remains coherent across the array. The position of subsidiary peaks in the array response depends on the particular geometry of the arrays. Early established seismic arrays often have simple geometric shapes geared to analog processing, but this leads to strong side lobes in array response, as recognized and analyzed by Birtill and Whiteway (1965). Most array processing is directed toward

suppressing the influence of side lobes on the response, so that the desired coherent signal is enhanced.

Many seismic arrays are based around circular configurations that give very good response, such as the ARCESS, NORESS, and GERESS regional arrays in Europe (e.g., Rost and Thomas, 2002). However, such configurations require a considerable number of stations. Recently Marano *et al.* (2014) presented a wide range of array designs based on an optimization procedure applied to the array response for a specified number of stations, with particular emphasis on the resolution of surface waves.

We present here a more pragmatic approach to array design based on a simple geometrical concept of spiral arms specified by a few parameters. Such arrays have been successfully implemented in both permanent and temporary configurations on a variety of scales.

Particularly strong sidebands in the array response arise when the station configuration has distinct alignments and symmetries and can be suppressed when symmetry is broken. A nested set of regular figures with increasing numbers of sides starting with a triangle, then a square, and so on, can be arranged to have no common symmetries. The array response is rather flat except for a central peak, as desired. As such array designs were tested, it was noted that the configuration resembled a set of spiral arms, and indeed the simpler spiral patterns had very desirable properties (Fig. 1).

Spiral-Arm Arrays

The configuration of an array with spiral arms is specified by (Fig. 1):

- the radial aperture of the array A (array radius),
- the number of arms n_a,
- the number of station rings n_r and their style of spacing, and
- the angular span associated with each arm Φ.

The spiral arms are set at regular spacing, with initial angle
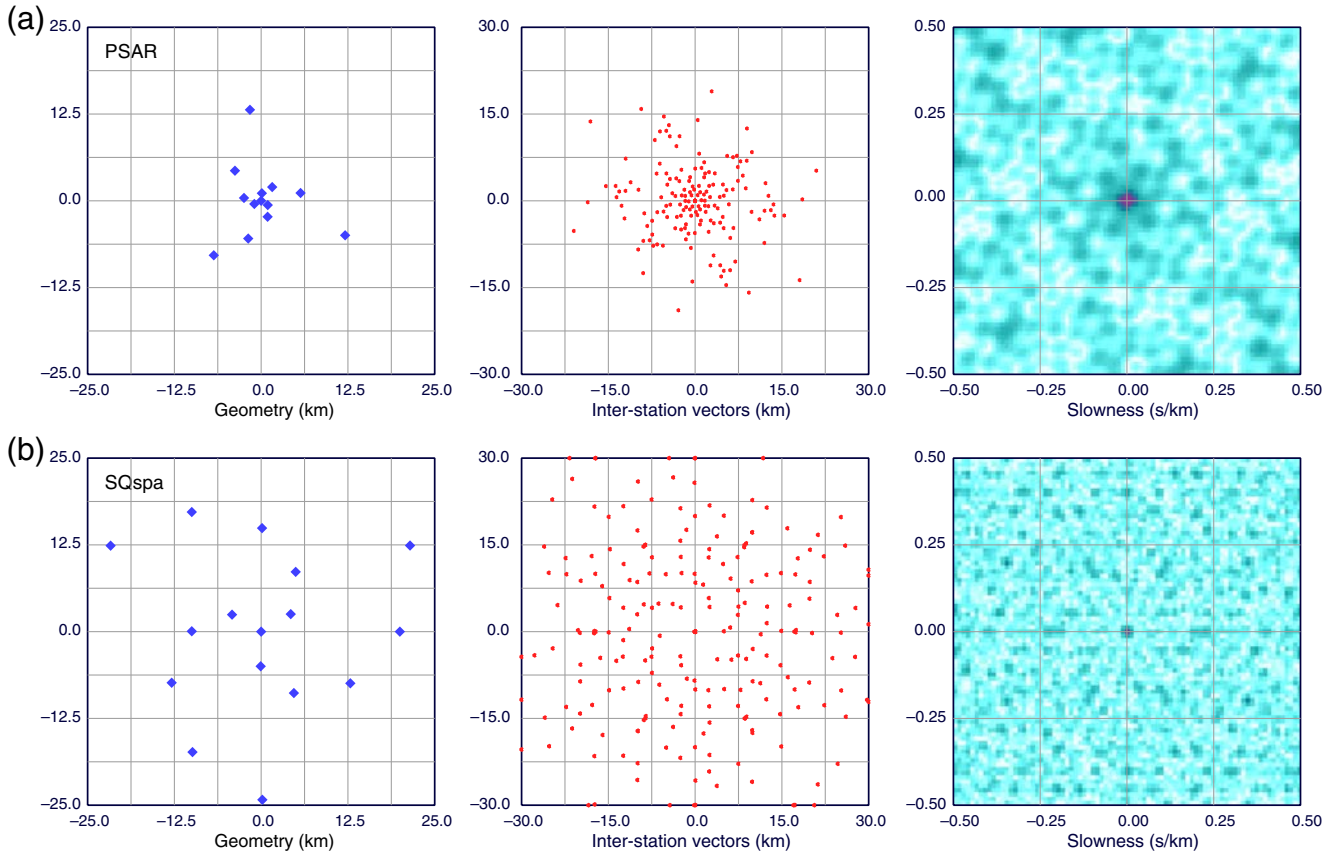
Figure 2. Configuration of the two broadband spiral-arm arrays deployed in Australia showing the array geometries on the same scale, the interstation vectors, and the array response at 1 Hz plotted with the same linear scale as in Figure 1: (a) The permanent Pilbara Seismic Array (PSAR) in the Pilbara craton of Western Australia installed on a single granite batholith. (b) The temporary SQspa array installed on ancient sediments in southern Queensland. The locations of the two arrays are shown in Figure 5. The color version of this figure is available only in the electronic edition.

$$\theta_{0k} = \vartheta_0 + 2\pi(k/n_a), \quad k = 1, \ldots, n_a, \quad (5)$$

for the kth arm. The constant ϑ_0 acts to rotate the pattern; for the example in Figure 1, $\vartheta_0 = \pi/6$. With regular ring spacing, the radius of the jth ring is

$$r_j = A(j/n_r), \quad j = 0, \ldots, n_r, \quad (6)$$

which includes a central station. If no central station is desired, then the index j starts from 1. The azimuth for the station on the jth ring of the kth arm is

$$\theta_{jk} = \theta_{0k} + \Phi(j/n_r). \quad (7)$$

The ring spacing can be usefully linked to the local wavefield coherence properties (Mykkeltveit *et al.*, 1983). We usually use three arms with a 120° angular span for each, with four or five rings, as illustrated in Figures 1 and 2.

The array response for such spiral patterns is good (Fig. 2), and robust to minor deviations from ideal design, as is inevitable in field implementation for arrays with apertures of many kilometers (see Ⓔ the electronic supplement to this article). For a cable installation, the spiral-arm configura-

tion minimizes the length of cable required, because it can follow each arm. For this reason, a spiral-arm configuration has been proposed for the central hubs of the Square Kilometre Array radio telescope, to be established from 2016 in southern Africa and Australia (see Data and Resources).

In radar antenna design, there have been considerable efforts to achieve high angular resolution without the need for a very large number of sensors. For example, Tang and Lu (2014) present a form of thinned array composed of a superposition of sparse arrays targeted at different levels of angular resolution. The spiral-arm design can be viewed as a comparable thinned array in 2D that emulates the performance of the dense multiring circular arrays deployed in Europe but with substantially fewer stations (see Ⓔ the electronic supplement).

A very wide class of array designs can be produced using the spiral-arm concept. We found that we can avoid configurations with strong symmetries by taking the angular span Φ to be $360/n_a$ degrees or a little larger. The stations in each ring have a symmetry dictated by the number of arms; however, at the next ring this pattern is rotated, so the sidebands are not consistent and even out to a modest level. When working with a limited number of stations, three-arm
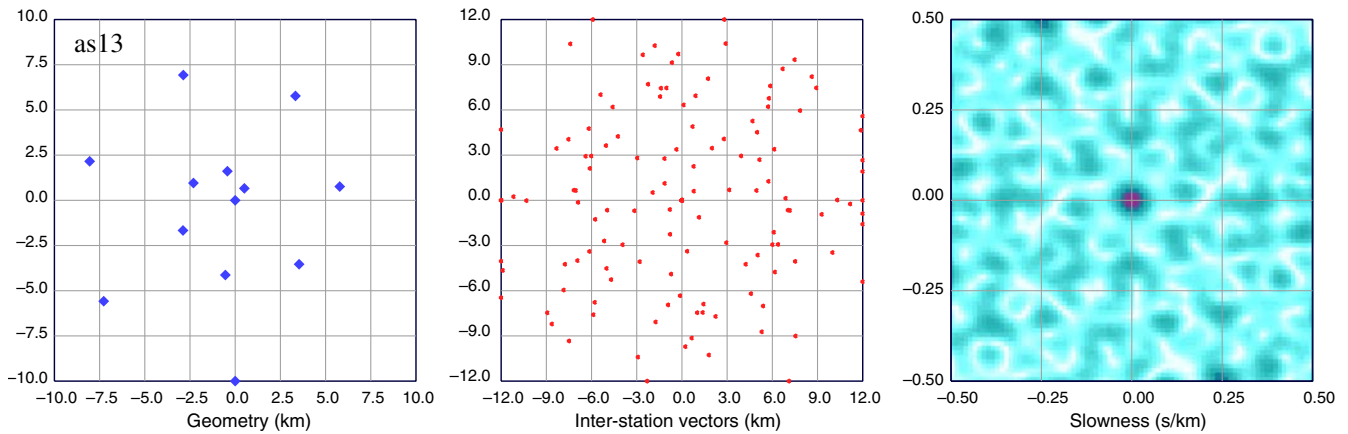
Figure 3. A 13-station Archimedean spiral-array design with the same 10 km maximum radius as in Figure 1, plotted at the the same scale. The array geometry is illustrated, along with the interstation vectors and the array response at 1 Hz plotted with the same linear scale as in Figure 1. The color version of this figure is available only in the electronic edition.

configurations work well and lend themselves to both linear and logarithmic ring spacing (Fig. 2). The inclusion of more spiral arms tends toward a space-filling design that is not economical on stations. The configurations illustrated in this article and in the Ⓔ electronic supplement have been tuned to minimize the sidebands in the response as far as possible for configurations with 10, 13, and 16 stations.

Medium-Scale Broadband Spiral-Arm Arrays

Two broadband arrays implementing the spiral-arm concept have been established in Australia. The Pilbara Seismic Array (PSAR), a permanent array in northwestern Australia was created by Geoscience Australia in the upgrade of the Australian network for enhanced tsunami warning. SQspa, a temporary array in southern Queensland, was deployed to experiment with multiarray processing techniques. Both arrays have broadband three-component sensors.

The 25-km-aperture PSAR has all stations in boreholes deployed on a single granite batholith in an Archean craton, with real-time telemetry to Canberra. For tsunami monitoring, the low-frequency signal is important, in addition to the higher frequency body-wave information for which regular beamforming can be used. The temporary array SQspa, with a larger aperture of 50 km, was sited on an ancient sedimentary basin, and array processing is undertaken after data recovery.

Figure 2 displays the configuration of the two arrays on the same scale, together with the patterns of interstation vectors, and the response in slowness space for a 1 Hz signal. In each case an excellent array response has been achieved with the three-arm spiral design with only a limited number of stations, certainly fewer than would be needed for a circular configuration with similar response (see Ⓔ the electronic supplement). For SQspa, the central peak is very tightly confined with a rapid drop-off, so only the minor side lobes are readily discerned.

Other Spiral-Array Configurations

Many other array concepts can be developed based on the different styles of spirals. Wathelet (2005) introduced an Archimedean spiral-array design that has rather low sidebands. We illustrate this concept in Figure 3 with a 13-station array, the same number of stations as in Figure 1, again with a 10 km maximum radius from the central station. For such a spiral, the distance between turnings is constant. The equation of the Archimedean spiral in polar coordinates is just $r = b\theta$, and we have taken stations at equal angular increments with a total span of 630°. This gives a concentration of stations near the center similar to the logarithmic station spacing for PSAR and a more sparse outer segment. Because the radial distance increases with station number, the effective aperture for the 13 stations is not as large as in the three-arm array in Figure 1, so the central peak is a little wider. The sidebands are quite low in amplitude but occur closer to the center than for the three-arm array of comparable radius.

A further class of array designs can be based on the logarithmic spiral $r = a \exp(b\theta)$, in which the spacing between turnings increases in geometric progression. An attractive feature of the logarithmic spiral is its self-similarity, and it is found in many natural forms such as the nautilus shell. With this form of spiral it is difficult to avoid overcrowding of stations near the center of the array. The exponential growth of the radius means that outer stations are widely separated. However, the logarithmic spiral could form the basis of an array designed for a very broad band of frequencies, in which different components of the array are used for selected frequency bands while still maintaining the same geometric relations between stations.

Direct Comparison of Array Geometries

To compare the effect of the different geometries we have considered directly, we show the array responses for all four designs with each array scaled to maximum radius 10 km
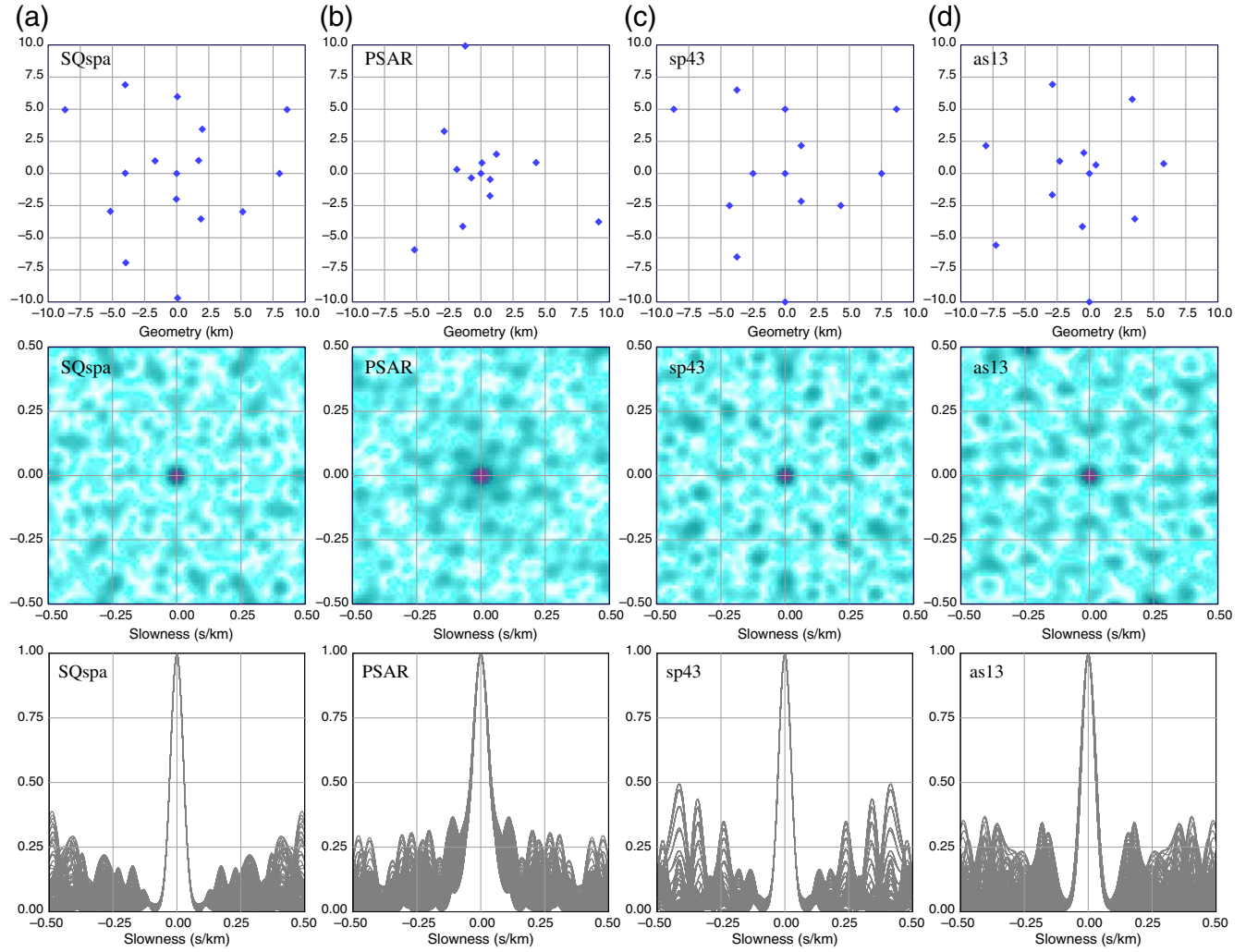
Figure 4. Comparison of geometries and array responses for the four arrays. The array sizes in the upper row have been normalized to the same 10 km maximum radius, so that the influence of the array geometries can be clearly seen. All array response plots in the middle row, calculated at 1 Hz, employ the same linear scale as in Figure 1. The lower row shows cross sections through the slowness response for a sweep of azimuths to illustrate the character of the central peak and side lobes. (a) Sixteen-element SQspa, three-arm array; (b) 13-element PSAR, three-arm array with logarithmic ring spacing; (c) 13-element s*p43*, three-arm design with linear ring spacing (as in Fig. 1); and (d) 13-element *as13*, Archimedean spiral design (as in Fig. 3). The color version of this figure is available only in the electronic edition.

from the central station, with the array geometry shown at the top (Fig. 4). We also include composite plots of azimuth cuts through the array response so that the nature of the central peak and side lobes can be seen more clearly.

The 16-element SQspa design, with three spiral arms, pushes the significant side lobes further from the origin in slowness than the other configurations (beyond 0.4 s/km). The minor modifications of station positions from the ideal plan in the field deployment have the effect of breaking symmetries and hence can sometimes improve array performance.

The 13-element PSAR design has a stronger station concentration near the center, and the siting requirements have led to a slightly asymmetric central peak. Sidebands of amplitude 0.30 abut the central peak, giving the hexagonal cell look to the array response, but all outer side lobes are a little smaller.

The 13-element spiral-arm design, with linear station spacing *sp43*, gives a tight central lobe and pushes all significant side lobes beyond 0.22 s/km from the central peak. This separation (25 s/°) is sufficient to avoid contamination of, for example, the core phase *PcP* by the *S* waves in the epicentral distance range where they overlap. However, in some directions, rather large sidebands occur for slownesses greater than 0.3 s/km. The improvement in sideband suppression achieved by adding an extra three elements, as in SQspa, is considerable.

For the 13-element Archimedean spiral *as13* there is, inevitably, an asymmetric central peak because of the one-sided distribution of the stations close to the origin. The outer sidebands stay at a very similar level, but the innermost ring of sidebands at around 0.15 s/km gives less room around the central peak than for the spiral-arm case. This means there
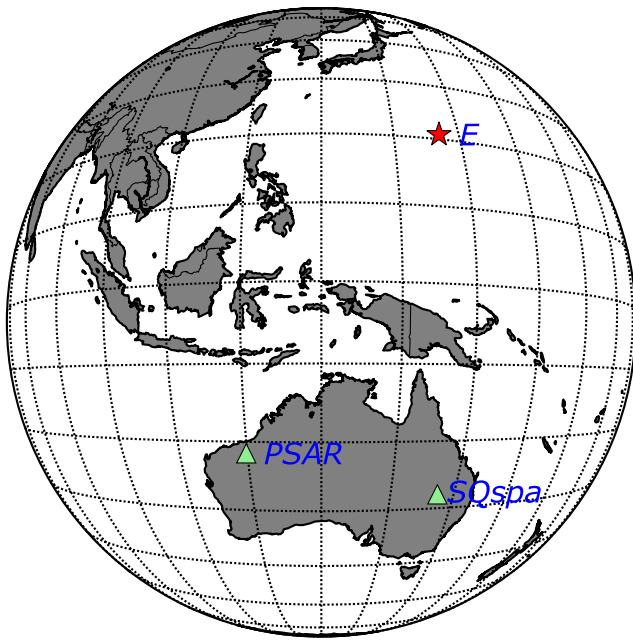
Figure 5.   Event and array configuration. The M_w 6.2 Mariana event on 17 December 2013, marked with a star, is located at 20.77° N, 146.79° E with a depth of 10 km. The color version of this figure is available only in the electronic edition.

is more possibility of interference from phases with slowness differing by more than 13 s/°, such as between mantle and core phases. We have also considered the case with 16-elements distributed over the same angular range for the single spiral; there is only modest change in the side lobe pattern with some suppression close to 0.3 s/km. The effect of adding the extra stations is much less than for the design with three spiral arms.

Practical Broadband Spiral-Arm Array Performance

The two broadband arrays, PSAR and SQspa, are based on a common concept but have rather different emplacement conditions. PSAR is a conventional hard-rock site with all stations in boreholes in a single granite batholith, and it employs expanding spacing between rings. SQspa has constant ring spacing with a larger aperture and sits on Mesozoic sediments. How do they compare in practice?

We have chosen an M_w 6.2 event in the Mariana arc recorded by both arrays at similar epicentral distances, around 48° (Fig. 5), and examine the vertical-component array records and stacks in Figure 6. We show the contoured array beams in 2D horizontal slowness space, as well as the seismograms at the individual elements of the array aligned on the P-wave arrival, and the linear stack for each array. The traces were band-pass filtered with corner frequencies 0.1 and 2 Hz. The frequency–wavenumber (f-k) analysis for the event at each array used a wide bandpass for a 30 s window around the P-phase onset.

The seismograms at the smaller-aperture PSAR show very similar characteristics at all elements of the array, but

the 25 km aperture of the array means that the resolution of the P-wave arrival in slowness and azimuth is limited. Nevertheless, there is a clear concentrated central peak near the expected vector slowness for the event (slowness 7.56 s/°, back azimuth 33.8°) for which we obtain a clear stack (Fig. 3). In contrast, at the larger SQspa array on a sedimentary basin, we see a little more variation in the timing of the arrivals, but still the first group of P-wave arrivals is very coherent, especially considering that interstation spacing is normally larger than 5 km. The coda shows a little more variation across the stations in the relative prominence of the later P-wave arrivals, but the stack is very clean. SQspa is slightly closer to the event, so the slowness of the beam peak is a little larger (7.65 s/°), and the back azimuth is very close to north (359.4°). Indeed the 50 km aperture of the array gives a very tight configuration in slowness–azimuth space for the maximum beam power of the P arrival, even though two stations in SQspa (SPR04 and SPR10) were not operational at the time of the Mariana event. For this event, deviations from the theoretical predictions are small, about 0.5 s/° for the extracted slowness and less than 6° in back azimuth. Such deviations are inevitable and depend strongly on structure in the neighborhood of the arrays.

We have assessed the signal-to-noise-ratio improvement at each array by looking at a 5 s interval of the noise before the P arrival and at the first 5 s of the P phase for a narrow frequency band from 0.5 to 1.5 Hz. For PSAR, the improvement in root mean square signal-to-noise ratio with the array stack is 2.4 compared with the average for the stations, and for SQspa it is 4.9. The results are encouraging relative to the theoretical improvement of the square root of the number of elements, 3.6 for PSAR and 4 for SQspa, which require fully correlated signals and uncorrelated noise.

Inspection of the seismogram windows indicates there is some degree of positive correlation of the noise just before P at the cratonic PSAR site in this 1 Hz band. This correlation tends to degrade the apparent stack enhancement, even though there is excellent coherence of the onset of P across the PSAR. For the larger-aperture SQspa temporary array on the old sedimentary basin, the stack enhancement is greater than expected despite the fact that the P arrivals show more variability across the array than at PSAR. Anticorrelation of the noise just before P at some sites strongly suppresses the noise stack, hence the signal stands out more clearly.

A significant merit of the spiral-arm design for seismic arrays is that array performance is very robust, both to the details of siting and to temporary failures in a few stations (see Ⓔ the electronic supplement). Logistic considerations rarely allow an array design to be implemented perfectly on the ground, and the tolerance of response of the spiral-arm arrays to minor variations in site position has allowed both PSAR and SQspa to adapt to local constraints and still achieve close to the expected theoretical resolution. We have shown the linear stack response because this is directly related to the geometry of the array, but enhancement of the precision of slowness estimates can readily be made by using nonlinear
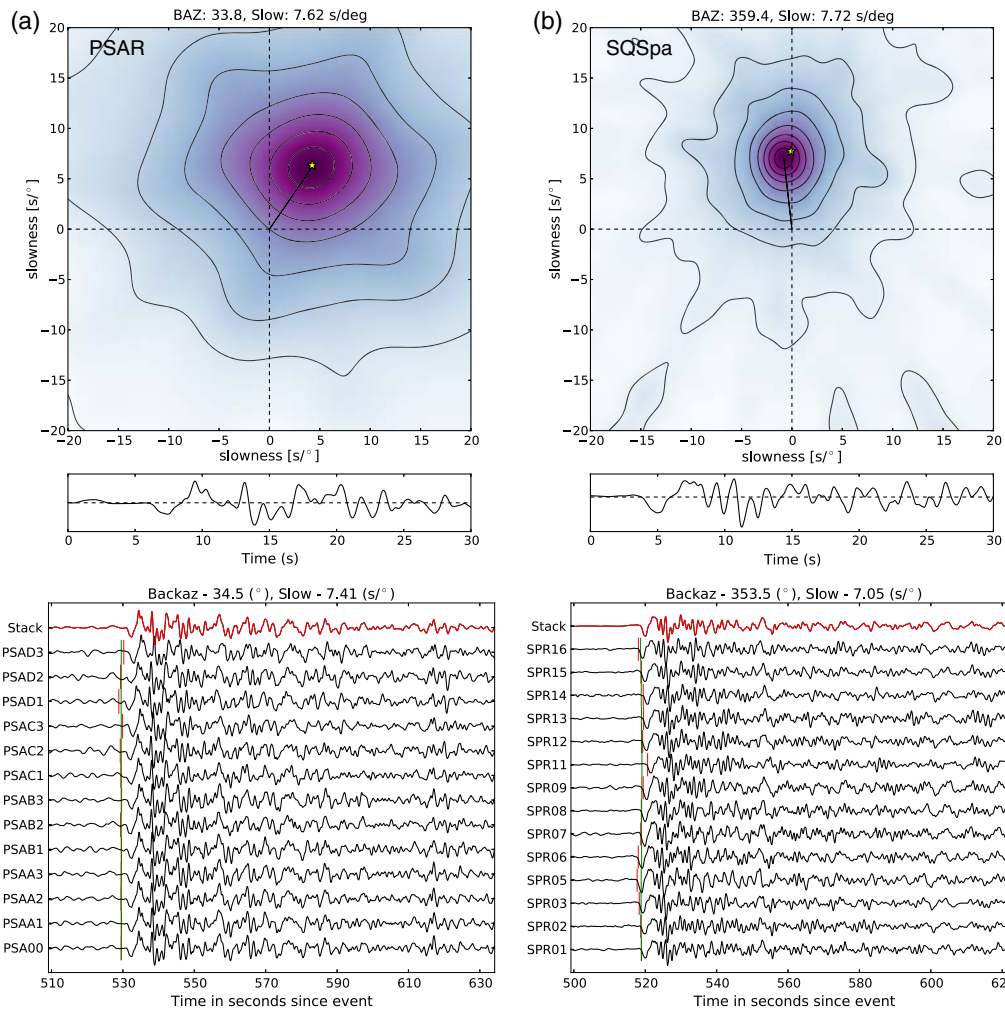
Figure 6. Comparison of slowness–azimuth determination via wavenumber stacking (i.e., frequency–wavenumber [*f-k*] analysis), seismograms, and array stacks for the M_w 6.2 Mariana event on 17 December 2013 (Fig. 3): (a) PSAR on hard-rock site in the Pilbara, Western Australia, epicentral distance 49.36°; and (b) SQspa array on ancient sediments in southern Queensland, epicentral distance 47.98°. Single traces at both arrays were first aligned on the *P* onset, and then stacking was performed over a range of beam parameters to produce the contoured displays in the upper panel. The offset vertical lines on the individual traces represent the onset times of the individual traces before alignment. The theoretical vector slowness for the ak135 model is indicated with a star (and at the top of the contour plots). The stacked trace for the theoretical slowness is shown below the slowness plots. The lower panels illustrate the nature of the *P* wavefield at the two arrays over a longer time span, together with the stacked trace using the peak beam power parameters (indicated at top of the trace plot). The color version of this figure is available only in the electronic edition.

stacking schemes that can exploit the vector character of the wavefield (e.g., Kennett, 2000; Gal *et al.*, 2014).

Small Arrays

In recent years, there has been a considerable expansion of interest in the use of small arrays for investigating shallower structure using seismic noise techniques. A popular approach is the spatially averaged coherency spectrum method exploiting ambient noise across an array, originally proposed by Aki (1957), due to its simplicity and low cost. The practical implementation of arrays for near-surface studies is a challenging task often guided by the number of available instruments and the configuration of the terrain. Spatial aliasing often limits the recovery of the short-wavelength part of the wavefield.

Short-term deployments can frequently be limited by access issues so that simple array geometries are often adopted with a limited available set of azimuthal orientations of station pair vectors. Where conditions allow, it is best to get away from such regular geometries (e.g. Marano *et al.*, 2014).

We have found considerable benefits in using the spiral-arm design in arrays up to a kilometer in diameter for frequencies from 0.5 to 5.0 Hz. As can be seen from Figure 2 and the examples in Ⓔ Figures S1 and S2, the distribution of interstation vectors and interstation distance achieved with the spiral-arm design is very good. This means that many directions and spacings can be achieved in a single deployment, providing good-quality surface-wave dispersion results that allow structural resolution of the near surface to depths > 300 m. The basic design employed is a 13-station configuration with four

regular-spaced rings on three spiral arms (*ar43* in Ⓔ Fig. S1). However, we found that even significantly distorted versions of the spiral-arm design provide good information, because there is an adequate coverage of azimuths. We investigated the most appropriate way to deploy the spiral-arm design using a travelling salesman algorithm (Applegate *et al.*, 2006) to optimize the process and found that following the line of the spiral arms minimizes the distances to be traversed in setting out and recovering the instruments.

Discussion and Conclusions

The spiral-arm array concept can be regarded as a thinned version of the successful concentric ring design. With many fewer stations, the class of design is well suited to temporary deployments using a limited number of instruments while still providing high slowness resolution and suppression of side lobes in the array response.

For regional and teleseismic studies, the success of a temporary deployment of the 50-km-aperture SQspa array on an ancient sedimentary basin opens new possibilities for a broader use of seismic arrays. Although hard-rock sites have commonly been favored, the geological environment in the neighborhood of larger arrays has often been found to be highly heterogeneous after the effort of deployment has been made. It is certainly possible to achieve homogeneity with modest aperture, as demonstrated by the PSAR in a single granite batholith of the Archean Pilbara craton, but such uniform features rarely exceed 20 km in size.

Larger arrays that can achieve much higher slowness and azimuth resolution may well perform better when sited on a broad sedimentary structure of rather uniform properties. There may be some attenuation of the highest frequencies, but these are rarely coherent across the entire array and so are not amenable to stacking methods. The spiral-arm array design is able to achieve high slowness and azimuth resolution with low sidebands using an economical number of stations and so is well suited to larger-aperture configurations.

The spiral-arm array design has also proven its worth in small-scale deployments, in which the resilience of the design and the good distribution of interstation vectors provide a good basis for surface-wave analysis.

Data and Resources

Seismograms from the Pilbara Seismic Array (PSAR) are freely available through the Incorporated Research Institutions for Seismology Data Management Center at ds.iris.edu with network code AU (last accessed November 2014). Additional information on the Square Kilometre Array radio telescope is accessible at http://www.skatelescope.org/layout/ (last accessed November 2014).

The data from the SQspa temporary deployment in Southern Queensland are archived at the Research School of Earth Sciences, Australian National University, and can be made accessible on request.

References

Aki, K. (1957). Space and time spectra of stationary stochastic waves, with special reference to microtremors, *Bull. Earthq. Res. Inst.* **25,** 415–457.

Applegate, D. L., R. E. Bixby, V. Chvátal, and W. J. Cook (2006). *The Traveling Salesman Problem: A Computational Study*, Princeton University Press, Princeton, New Jersey, 606 pp.

Birtill, J. W., and F. E. Whiteway (1965). The application of phased arrays to the analysis of seismic body waves, *Phil. Trans. Roy. Soc. London* **258,** 421–493.

Gal, M., A. M. Reading, S. P. Ellingsen, K. D. Koper, S. J. Gibbons, and S. P. Nasholm (2014). Improved implementation of the *f-k* and Capon methods for array analysis of seismic noise, *Geophys. J. Int.* **198,** 1045–1054.

Kennett, B. L. N. (2000). Stacking 3-component seismograms, *Geophys. J. Int.* **141,** 263–269.

Kennett, B. L. N. (2002). *The Seismic Wavefield II—Interpretation of Seismograms on Regional and Global Scales*, Cambridge University Press, Cambridge, United Kingdom.

Marano, S., D. Fäh, and Y. M. Lu (2014). Sensor placement for the analysis of seismic surface waves: Sources of error, design criterion and array design algorithms, *Geophys. J. Int.* **197,** 1566–1581.

Mykkeltveit, S., K. Åstebøl, D. J. Doornbos, and E. S. Husebye (1983). Seismic array configuration optimisation, *Bull. Seismol. Soc. Am.* **73,** 173–186.

Rost, S., and C. Thomas (2002). Array seismology: Methods and applications, *Rev. Geophys.* **40,** no. 3, 2-1–2-27, doi: 10.1029/2000RG000100.

Tang, Y., and Y. Lu (2014). Multi-resolution composite array for digital beamforming with high angular-resolution, *IEEE Trans. Antenn. Propag.* **62,** 4377–4380, doi: 10.1109/TAP.2014.2323427.

Wathelet, M. (2005). Array recordings of ambient vibrations: Surface-wave inversion, *Doctor of Applied Science Thesis*, University of Liége, available from http://sesame.geopsy.org/Papers/These-Wathelet_2005.pdf (last accessed November 2014).

Research School of Earth Sciences
The Australian National University
Canberra ACT 2601, Australia
Brian.Kennett@anu.edu.au
Josip.Stipcevic@anu.edu.au
        (B.L.N.K., J.S.)

Geoscience Australia
GPO Box 378
Canberra ACT 2601, Australia
Alexei.Gorbatov@ga.gov.au
        (A.G.)